# Pion form factor and charge radius from Lattice QCD at physical point

Xiang Gao,[1, 2, *] Nikhil Karthik,[3, 4] Swagato Mukherjee,[1] Peter Petreczky,[1] Sergey Syritsyn,[5, 6] and Yong Zhao[7, 1]

[1]*Physics Department, Brookhaven National Laboratory, Upton, NY 11973, USA*
[2]*Physics Department, Tsinghua University, Beijing 100084, China*
[3]*Department of Physics, College of William & Mary, Williamsburg, VA 23185, USA*
[4]*Thomas Jefferson National Accelerator Facility, Newport News, VA 23606, USA*
[5]*Department of Physics and Astronomy, Stony Brook University, Stony Brook, NY 11794, USA*
[6]*RIKEN-BNL Research Center, Brookhaven National Lab, Upton, NY, 11973, USA*
[7]*Physics Division, Argonne National Laboratory, Lemont, IL 60439, USA*
(Dated: February 10, 2021)

We present our results on the electromagnetic form factor of pion over a wide range of $Q^2$ using lattice QCD simulations with Wilson-clover valence quarks and HISQ sea quarks. We study the form factor at the physical point with a lattice spacing $a = 0.076$ fm. To study the lattice spacing and quark mass effects, we also present results for 300 MeV pion at two different lattice spacings $a = 0.04$ and $0.06$ fm. The lattice calculations at the physical quark mass appear to agree with the experimental results. Through fits to the form factor, we estimate the charge radius of pion for physical pion mass to be $\langle r_\pi^2 \rangle = 0.41(2)$ fm$^2$.

## I. INTRODUCTION

Pion is one of the most prominent strongly interacting particle next to the nucleon since it is a Goldstone boson of QCD. For this reason it is important to study the pion internal structure and find out if there is a connection between its internal structure and its Goldstone boson nature. This issue is particularly relevant for understanding the origin of mass generation in QCD, see e.g. discussions in Refs. [1, 2].

The knowledge of internal structure of the pion is much more limited than that of the nucleon. On the partonic level the parton distribution function (PDF) of the pion can been studied through the global analysis of the Drell-Yan production in pion-nucleon collisions and in tagged deep inelastic scattering (DIS), for recent analyses see Refs. [3, 4]. Recently there have been many efforts in lattice QCD to study the pion PDF [5–10] which use the quasi-PDF in Large Momentum Effective Theory [11, 12], the pseudo-PDF [13, 14] and current-current correlator [15–17] (also referred to as good lattice cross section) approaches, see Refs. [18–21] for recent reviews. Lattice calculations of the lowest moments of pion PDF [22–27] are also available and can be used as additional constraints in the global analysis.

Form factor, defined as

$$\langle P_1 | J_\mu | P_2 \rangle = (P_1 + P_2)_\mu F_\pi(Q^2), \qquad (1)$$

with $J_\mu$ being the electro-magnetic current and $Q^2 = (P_2 - P_1)^2$, provide a different insight into pion structure, namely the charge distribution. It can be in principle measured in electron pion scattering. Generalized parton distribution (GPD) combine the information contained in PDF and form factors and provide a three-dimensional image of a hadron. In the case of the nucleon the study of GPD is the subject of large experimental and theory efforts (see e.g. Ref. [28] for a recent review). The experimental study of the pion GPD is far more challenging and will be only possible at Electron-Ion Collider (EIC), if at all. Fortunately GPDs can be studied on the lattice using LaMET, including pion GPDs [29–32].

Experimentally, the pion form factor was measured by scattering of pions off atomic electrons in Fermilab [33, 34] and CERN [35, 36]. This allowed to determine the pion form factor for momentum transfer $Q^2$ up to 0.253 GeV$^2$ [33–36]. For larger $Q^2$ one has to determine the pion form factor from the electro-production of charged pions off nucleons. The corresponding experiments have been performed in Cornell [37–39] DESY [40, 41], and Jlab [42–46] This determination, however, is model dependent. Recent determination of the pion form factor up to $Q^2$ of 2.45 GeV$^2$ been carried out by the $F_\pi$ collaboration using data both from DESY and JLab [46]. Experiments at the future EIC facility will allow to probe even higher $Q^2$ up to 30 GeV$^2$ and possibly see the partonic structure in a exclusive elastic process and make contact with asymptotic large $Q^2$ perturbative behavior [47].

Lattice QCD calculations allow to obtain the pion form factor from first principles, i.e. without any model dependence, up to relatively large $Q^2$. Therefore, they will provide an important cross-check for the experimental determinations. The first lattice calculations of the pion form factor date back to late 80s and have been performed in the quenched approximation [48, 49]. More recently lattice calculations of the pion form factor have been performed with two flavors ($N_f = 2$) of dynamical quarks [50–54], with physical strange quark and two light quark flavors ($N_f = 2+1$) [55–61], as well as with dynamical charm quark, strange quark and two flavors of the light quarks with nearly physical masses ($N_f = 2+1+1$) [62]. Most of the lattice studies focused on the small $Q^2$ behavior of the pion form factor and the extraction of

the pion charge radius. The pion charge radius is very sensitive to the quark mass. The chiral perturbation theory predicts a logarithmic divergence of the pion charge radius when quark mass goes to zero [63]. Therefore, one has to work at physical quark mass or have calculations performed in an appropriate range of quark masses to perform chiral extrapolations. Furthermore, studies have been performed for lattice spacing $a > 0.09$ fm.

The aim of this paper is to study the pion form factor in a wide range of $Q^2$. Therefore, we perform calculations for small lattice spacings, namely $a = 0.04$fm and $0.06$ fm with valence pion mass of about 300 MeV. Furthermore, to study quark mass effect we also perform calculations at the physical pion mass, though at somewhat larger lattice spacing, $a = 0.076$ fm. Unlike previous studies we also perform calculations for highly boosted pion in order to extend them in the future for the pion GPD.

## II. LATTICE SETUP

In this study we use Wilson-Clover action with hypercubic (HYP) [64] smearing on 2+1 flavor staggered $L_t \times L_s^3$ lattices generated with highly improved staggered quark (HISQ) action by HotQCD collaboration [65, 66]. For the clover coefficient we use the tree-level tadpole improved value $c_{sw} = u_0^{-3/4}$, with $u_0$ being the HYP smeared plaquette expectation value. This setup is the same as the one used by us to study the valence parton distribution of the pion [9, 10]. As in Refs. [9, 10] we use two lattice spacings $a = 0.04$ fm and $a = 0.06$ fm and the valence pion mass of 300 MeV. The lightest pion mass for these gauge configurations is $m_\pi^{sea} = 160$ MeV and the lattice spacings was fixed through $r_1$ scale [65] using the value $r_1 = 0.3106(18)$ fm [67]. In addition, we performed calculations at a lattices spacings of 0.076 fm and valence pion mass of 140 MeV using the gauge configurations that correspond to the lightest pion mass of $m_\pi^{sea} = 140$ MeV [66]. The lattice spacings was set by the kaon decay constant, $f_K$ [66]. The lattice ensembles used in this study and the corresponding parameters are summarized in Table I. Because of the use of the HISQ action the taste splitting in the pion sector is small for lattice spacings $a < 0.076$ fm. The root mean square pion mass is only 15% than the lightest pion mass, while the heaviest pion mass is only 25% above the lightest pion mass [66]. In what follows for $a = 0.076$ fm ensemble will will not make a difference between the sea and the valence pion mass and refer to this ensemble as $m_\pi = 140$ MeV ensemble or the ensemble with physical pion mass. The effects of partial quenching will persist at finite lattice spacings but will go away in the continuum limit.

To obtain the form factor we calculate the pion two-point and three point functions. We consider two point functions defined as

$$C_{2\text{pt}}^{ss'}(t; P_z) = \left\langle \pi_s(\mathbf{P}, t)\pi_{s'}^\dagger(\mathbf{P}, 0) \right\rangle, \qquad (2)$$

where $\pi_s(\mathbf{P}, t)$ are either smeared or point sources, $s = S, P$ sources with spatial momentum

$$\mathbf{P} = \frac{2\pi}{aL_s} \cdot (n_x, n_y, n_z).$$

As in the previous studies [9, 10] we used boosted Gaussian sources in Coulomb gauge with boost along the $z$-direction $k_z = 2\pi/L_s \cdot (0, 0, j_z)$. The radius of the Gaussian sources $r_G$ is also given in Table I. The three-point function is defined as

$$C_{3\text{pt}}(\mathbf{P}^f, \mathbf{P}^i, \tau, t_s) = \left\langle \pi_S(\mathbf{P}^f, t_s)O_{\gamma_t}(\tau)\pi_S^\dagger(\mathbf{P}^i, 0) \right\rangle, \quad (3)$$

with

$$O_{\gamma_t}(\tau) = \sum_{\mathbf{x}} e^{-i(\mathbf{P}^f - \mathbf{P}^i)\mathbf{x}} \left[ \overline{u}(x)\gamma_t u(x) - \overline{d}(x)\gamma_t d(x) \right], \ x = (\mathbf{x}, \tau)$$
$$(4)$$

being the iso-vector component of the electric charge operator. Note that the iso-singlet component of the electric charge vanishes between the pion states. The initial momentum in the above expression is $\mathbf{P}^i = 2\pi/(aL_s) \cdot (0, 0, n_z)$, while the final momentum is $\mathbf{P}^f = \mathbf{P} = \mathbf{P}^i + \mathbf{q}$. The values of the momenta used in this study as well as the corresponding boost parameter $j_z$ are summarized in Table I. We calculated the three point functions for three values of the source-sink separations, $t_s$ for the two coarser lattices. For the finest lattice we used four source-sink separations. The source think separations used in our study are also listed in Table I.

The calculations of the two and three point functions were performed on GPU, with the QUDA multi-grid algorithm used for the Wilson-Dirac operator inversions to get the quark propagators. We used many sources together with All Mode Averaging (AMA) technique [68] to increase the statistics. The stopping criterion for AMA was set to be $10^{-10}$ and $10^{-4}$ for the exact and sloppy inversions respectively. Since the signal is deteriorating with increasing momenta we use different number of sources and number of gauge configurations for different momenta. The number of gauge configurations and number of sources used in the analysis are given in the last two columns of Table I for each value of the momenta.

For the study of the form-factor it is useful to use the Breit frame, where $|\mathbf{P}^i| = |\mathbf{P}^f|$. The use of the Breit frame is essential when studying the GPD within LaMET [29–32]. Therefore we also calculated the pion form factor using the Breit frame. The parameters of this set-up are summarized in Table II.

## III. TWO-POINT FUNCTION ANALYSIS

Since the source-sink separation used in this study are not very large it is important to quantify the contributions of the excited states when extracting pion matrix elements. This in turn requires a detailed study of the pion two point functions. For $a = 0.04$ fm and 0.06 fm

3

| Ensemble: | $m_\pi^{val}$ (GeV) | $c_{sw}$ | $t_s/a$ | $r_G$ fm | $n_z$ | $n_i$ $(i=x,y)$ | $j_z$ | #cfgs | (#ex,#sl) |
|---|---|---|---|---|---|---|---|---|---|
| $a = 0.076$ fm, $m_\pi sea = 0.14$ GeV, $64 \times 64^3$ | 0.14 | 1.0372 | 6, 8, 10 | 0.342 | 0,1 | ±1,±2 | 0 | 350 | (5, 100) |
| | | | | | 2,3 | ±1,±2 | 1 | 350 | (5, 100) |
| $a = 0.06$ fm, $m_\pi^{sea} = 0.16$ GeV, $64 \times 48^3$ | 0.3 | 1.0336 | 8, 10, 12 | 0.312 | 0,1 | ±1,±2 | 0 | 100 | (1, 32) |
| | | | | | 2,3 | ±1,±2 | 1 | 525 | (1, 32) |
| $a = 0.04$ fm, $m_\pi^{sea} = 0.16$ GeV $64 \times 64^3$ | 0.3 | 1.02868 | 9,12, 15,18 | 0.208 | 0,1 | ±1 | 0 | 314 | (3, 96) |
| | | | | | 0,1 | ±2 | 0 | 314 | (2, 64) |
| | | | | | 2,3 | ±1 | 1 | 564 | (4, 128) |
| | | | | | 2,3 | ±2 | 1 | 564 | (3, 96) |

TABLE I. The lattice parameters used in our calculations. Shown are the gauge ensembles used in our study, the valence pion mass, the coefficient of the clover term, the size of the smeared Gaussian sources, the source-sink separations, used in the analysis of the three point functions, the value of the momenta and with the corresponding boost parameters, see text. The last two columns show the number of gauge configurations and the number of sources in AMA, see text.

| Ensemble $a, L_t \times L_s^3$ | $m_\pi$ (GeV) | $t_s/a$ | $n_z^p$ | $n_i^p$ $i=x,y$ | $n_i^q$ $i=x,y$ | #cfgs | (#ex,#sl) |
|---|---|---|---|---|---|---|---|
| $a = 0.06$ fm, $64 \times 48^3$ | 0.3 | 8, 10 | 2 | ±1 | ∓2 | 120 | (1, 32) |
| $a = 0.04$ fm, $64 \times 64^3$ | 0.3 | 9,12, 15,18 | 2 | ±1 | ∓2 | 120 | (1, 32) |

TABLE II. Two set of the measurements in the Breit frame of 2 ensembles are shown. Using the similar notation like Table I, the initial pion have transverse momentum $P_\perp^i = 2\pi n_i^p/(L_s a)$, and final state $\mathbf{P}^f = \mathbf{P}^i + \mathbf{q}$ have the same energy.

lattices and $m_\pi^{val} = 300$ MeV the pion two point functions have been studied for different momenta along the $z$-direction in Refs. [9, 10]. Furthermore, this analysis was very recently extended to include momenta also along the $x$ and $y$-directions for $a = 0.04$ fm [69]. We extended this analysis to $a = 0.076$ fm and the physical pion mass.

The pion two point function in Eq. (2) has the spectral decomposition:

$$C_{2pt}^{ss'}(t) = \sum_{n=0}^{N_{state}-1} A_n^s A_n^{s'*}(e^{-E_n t} + e^{-E_n(aL_t-t)}), \quad (5)$$

where $E_{n+1} > E_n$, with $E_0$ being the mass of the pion ground state. $A_n$ is the overlap factor $\langle \Omega | \pi_s | n \rangle$ of the state $n$ and the state created by operator $\pi_s$ from the vacuum state $|\Omega\rangle$. Thanks to the Gaussian smearing, the excited state contribution is suppressed. So we truncate the Eq. (5) up to $N_{state} = 3$ and then fit the data in a range of $t$ between $[t_{min}, aL_t/2]$. The one-state fit results of the smeared-smeared (SS) two point function are shown in left panels of Fig. 1 for three different momenta. As one can see, the ground state energies, $E_0$ reach a plateau when $t_{min} \gtrsim 10a$. And at $\mathbf{P} = 0$, the plateau is around $m_\pi = 140$ MeV, which is the physical pion mass. The lines in the plots are computed from the dispersion relation $E_0(\mathbf{P}) = \sqrt{\mathbf{P}^2 + m_\pi^2}$, and show good consistency with the plateaus. Thus for the determination of the next energy level, we can fix the ground state energy $E_0$ to be from the dispersion relation, and perform a 2-state fit. Interestingly, as shown in right panels of Fig. 1,

we can also observe plateaus for $E_1$ when $t_{min} > 5a$, following the dispersion relation $E_1(\mathbf{P}) = \sqrt{\mathbf{P}^2 + m_{\pi'}^2}$ well within the errors. This could imply a single-particle excited state, namely the first radial excitation of the pion $\pi(1300)$ [69]. Since the first excited state energy, $E_1$ does not reach a plateau for $t_{min} < 5a$, we conclude that for $t/a < 5$ the contribution of higher excited states in the two point function is significant. Therefore, we need to consider three state fits for these $t$ values. To perform the three state fit, we fix $E_0$ to the dispersion relation and put a prior to $E_1$ using the best estimates from SS and smeared-point (SP) correlators [10] together with the errors from the two-state fit. This way we get the third excited state energy, $E_2$, which does not depend on $t_{min}$ within the statistical errors. However, the value of $E_2$ is very large, about 3 GeV. This implies that $E_2$ does not actually belong to a single energy state but rather to a tower of many higher excited states. The situation is similar for other two 300 MeV ensembles [10].

Now we understand that a two-state spectral model can describe our two-point functions well when $t_{min} \gtrsim 5a$, while three-state can describe $t_{min} \gtrsim 2a$. This will be important to keep in mind when analyzing the three point function and pion matrix elements in the next section. To summarize this section, in Fig. 2 we show the dispersion relation obtained from the above analysis. We also extended the analysis for $a = 0.06$ fm [10] by including additional momenta with non-zero components along the $x$ and $y$-directions. The corresponding results are also shown in Fig. 2. We clearly see the effect of
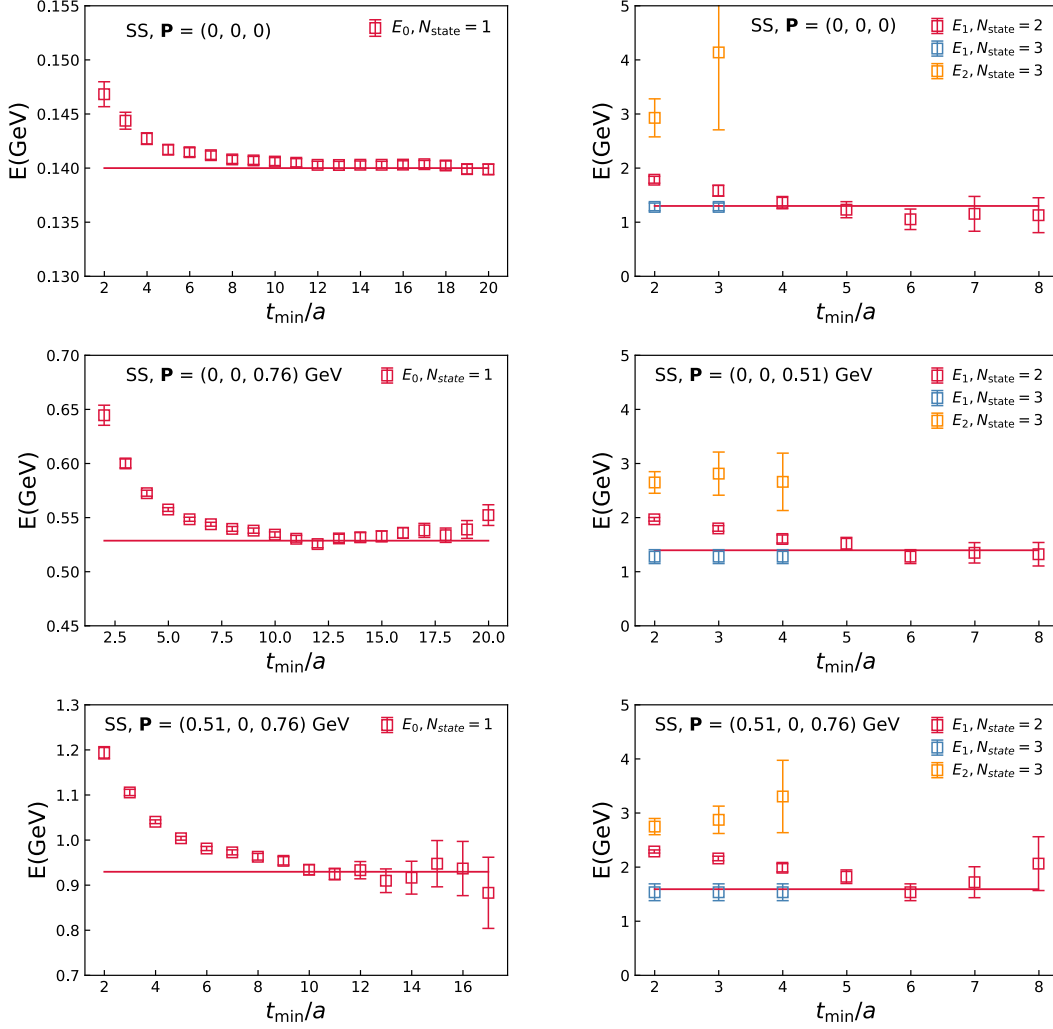
FIG. 1. $E_0$ from one-state fit (left) and $E_1$, $E_2$ from constrained two-state and 3-state fit (right) for three different momentum are showed as a function of $t_{\min}$. The lines are computed from the dispersion relation $E(\mathbf{P}) = \sqrt{\mathbf{P}^2 + E(\mathbf{P} = 0)^2}$, with $E(\mathbf{P} = 0)$ to be 0.14 GeV for $E_0$ and 1.3 GeV for $E_1$. As can be observed, the $E_0$ and $E_1$ reach a plateau for large enough $t_{\min}$.

the quark masses. For the physical pion mass the first excited state has the correct mass of $\pi(1300)$, while for the larger quark mass ($a = 0.06$ fm) the excited state is about 200 MeV higher.

## IV. EXTRACTION OF BARE MATRIX ELEMENT OF PION GROUND STATE

To obtain the bare pion form factor we consider the following standard ratio of the three point and two point pion functions [70]

$$
\begin{aligned}
R^{fi}(\tau, t_s) &\equiv \frac{2\sqrt{P_0^f P_0^i}}{P_0^f + P_0^i} \frac{C_{3\text{pt}}(\mathbf{P}^f, \mathbf{P}^i, \tau, t_s)}{C_{2\text{pt}}(t_s, \mathbf{P}^i)} \\
&\times \left( \frac{C_{2\text{pt}}(t_s - \tau, \mathbf{P}^f) C_{2\text{pt}}(\tau, \mathbf{P}^i) C_{2\text{pt}}(t_s, \mathbf{P}^i)}{C_{2\text{pt}}(t_s - \tau, \mathbf{P}^i) C_{2\text{pt}}(\tau, \mathbf{P}^f) C_{2\text{pt}}(t_s, \mathbf{P}^f)} \right)^{1/2}
\end{aligned}
\tag{6}
$$

This ratio gives the bare pion form factor in the limit $t_s \to \infty$: $h_B(P_f, P_i) = \lim_{t_s \to \infty} R^{fi}(\tau, t_s)$.

As explained in Sec. II, we calculated the three-point functions with $\mathbf{P}^i$ along with $z$ direction, and multiple momentum transfer $\mathbf{q} = \mathbf{P}^f - \mathbf{P}^i$ for each $\mathbf{P}^i$. Thus there is no difference for $\mathbf{q}$ with same magnitude of the transverse momentum transfer. In other words, there should be transverse symmetry for the three-point function data. We find that indeed that our numerical results for $R^{fi}(\tau, t_s)$ with same $|n_x^q|$ and $|n_y^q|$ are consistent within the error. Therefore, we average the three-point functions data with same magnitude of the transverse momentum transfer in the following analysis.

Since the temporal extent of our lattices is not large it is important to consider thermal contamination, also called wrap-around effects, caused by the periodic boundary condition [10]. To remove the wrap-around effects in the two point function we replaced $C_{2\text{pt}}(t)$ by
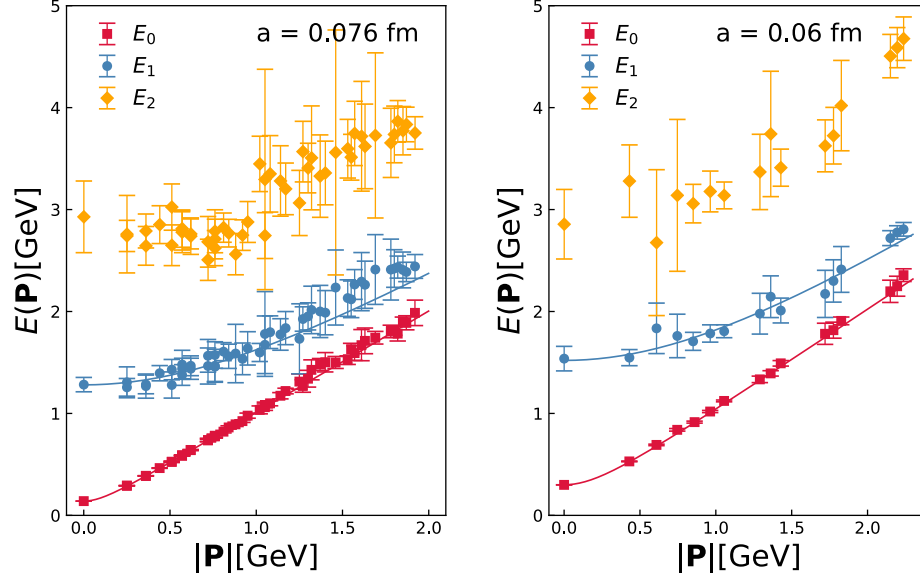
FIG. 2. Dispersion relation determined by the plateau of Fig. 1 for the physical pion mass ensemble (left) and a = 0.06 fm ensemble (right). The lines are dispersion relation calculated by $E(\mathbf{P}) = \sqrt{\mathbf{P}^2 + E(\mathbf{P}=0)^2}$.

$C_{2\text{pt}}(t) - A_0 e^{-E_0(aL_t-t)}$ using the best estimate of $A_0$ and $E_0$ from the 2-point function analysis. To understand wrap-around effects in the three point function we consider the spectral decomposition of $C_{3\text{pt}}$ in Eq. (6)

$$
\begin{aligned}
&\langle \pi_S(\mathbf{P}^f, t_s) O_{\gamma_t}(\tau) \pi_S^\dagger(\mathbf{P}^i, 0) \rangle \\
&= \sum_{m,n,k} \langle m|\pi_S|n\rangle \langle n|O_{\gamma_t}|k\rangle \langle k|\pi_S^\dagger|m\rangle \times \\
&e^{-\tau E_k} e^{-(t_s-\tau)E_n} e^{-(aL_t-t_s)E_m},
\end{aligned}
\tag{7}
$$

where $m, n, k = \Omega,\ 0,\ 1,\ \ldots$, with 0 being the pion ground state. In general, terms with non-zero $E_m$ will be highly suppressed by $e^{-(aL_t-t_s)E_m}$ (we assume $E_\Omega = 0$). Therefore, in most studies such terms are neglected. For $P = 0$ case $e^{-(aL_t-t_s)E_m(P=0)} = e^{-aL_t m_\pi}$, however, is not very small. We have $e^{-aL_t m_\pi} \sim 0.03, 0.003, 0.02$ for a = 0.076, 0.06 and 0.04 fm lattices, respectively. On the other hand, for non-zero momenta the terms proportional to $e^{-(aL_t-t_s)E_m}$ are smaller than 0.003 and can be neglected. Therefore, for a = 0.04 fm and 0.076 fm calculations we only consider non-zero momenta and limit the sum over index $m$ in Eq. (7) to include only the vacuum state in what follows. We need, however, to consider the wrap-around effects when dealing with the renormalization, as discussed in the next section.

In this work, we use multi-state fit to extract the bare matrix elements of the ground state $\langle P^f|O_{\gamma_t}|P^i\rangle \equiv \langle 0P^f|O_{\gamma_t}|P^i 0\rangle$ by inserting the spectral decomposition of the two point function in Eq. (5) and the three point function in Eq. (7) with $m = \Omega$, and the sum over $n$ truncated to $N_{state}$ terms. Furthermore, we take the best estimate of $A_n$ and $E_n$ from the two-point function analysis. and put them into Eq. (6). In the following we will refer

to this method as Fit($N_{state}, n_{sk}$), in which $N_{state}$ is the number of states in the corresponding 2-point function analysis and $n_{sk}$ labels how many $\tau$ we skipped on the two sides of $t_s$. We consider $N_{state} = 2$ and $N_{state} = 3$ that imply four and nine fit parameters, respectively.

In Fig. 3, we show the examples of ratio $R^{fi}(\tau, t_s)$ as well as the 2-state and 3-state fit results. As one can see, for large momentum, the 2-state and 3-state fit results are consistent with each other because of the large statistical errors, while this is not the case for smaller momentum, where the data are more precise. The 3-state fit can describe the data on the ratio data better than the 2-state fit. Thus for the following analysis, we will take the 3-state fit results as the central value and use the corresponding statistical errors. However, even when using 3-state fit there is no guarantee that we are free from excited state contamination. Therefore, we take the difference between 2-state fit and 3-state fit results as the systematic errors in the following analysis.

## V. THE PION FORM FACTORS

To obtain the form factor from the bare form factor determined in the previous section it needs to be multiplied by the vector current renormalization factor, $Z_V$. The simplest way to obtain this is to calculate the forward matrix element $h_B(P^i, P^i) = \langle 0P^i|O|P^i 0\rangle = Z_V^{-1}$. one needs to keep in mind the wrap-around effect discussed in the previous section. The other issue is cutoff dependence of $h_B(P^i, P^i)$ at large values of $P^i$. In Fig. 4, we show $h_B(P^i, P^i)$ for a = 0.076 fm as function of $(aP^i)$. In absence of discretization effects $h_B(P^i, P^i)$ should be independent of $P^i$ since after renormalization
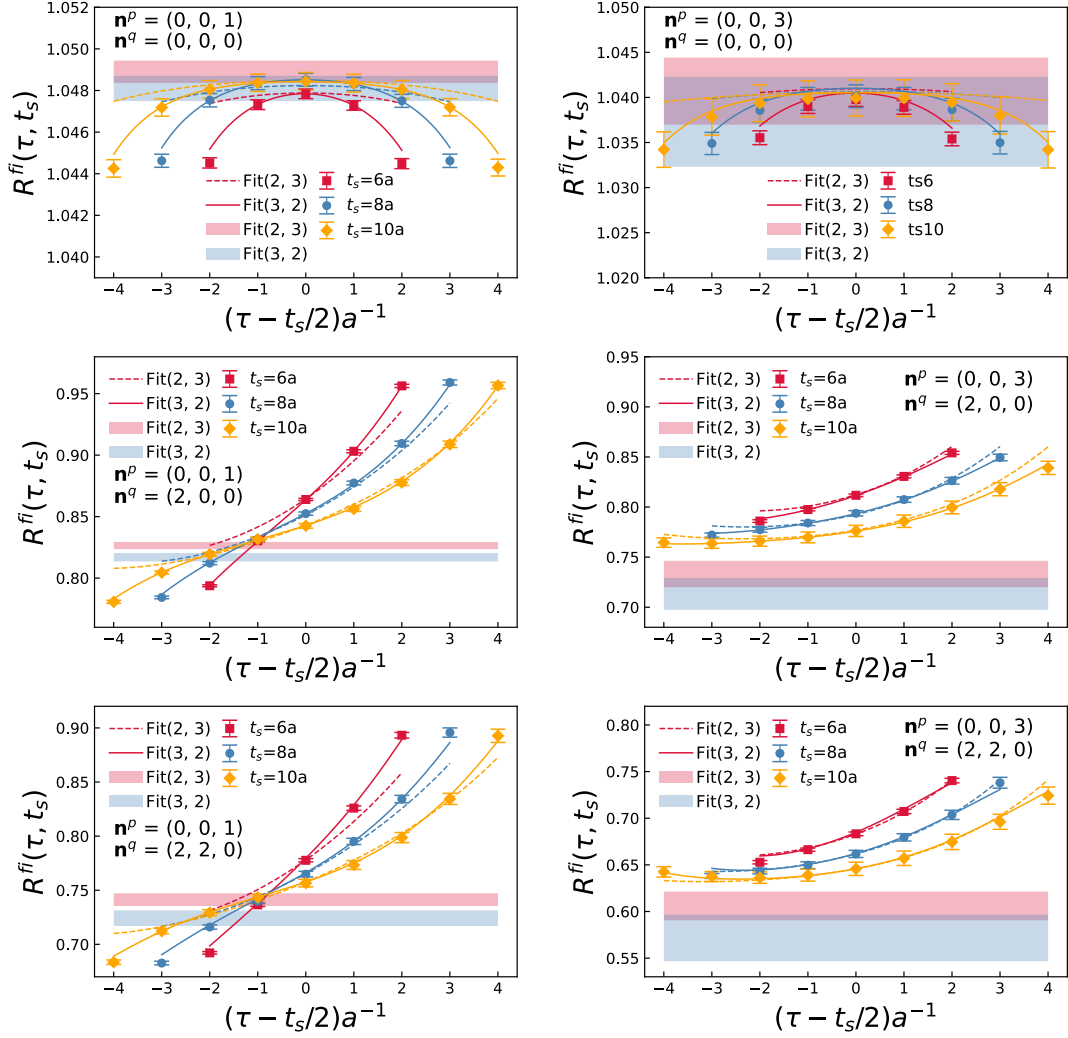
FIG. 3. $R^{fi}(\tau, t_s)$ for $\mathbf{n^P}_i = (0,0,1)$ (left) and $(0,0,3)$ (right) for $\mathbf{n^q} = (0,0,0), (2,0,0), (2,2,0)$ of physical ensemble are shown. The curves are the central value of multi-state fit Fit(2,3) (dashed) and Fit(3,2) (solid), and the bands are the estimated bare matrix elements.

it gives the charge of the pion. In other words $Z_V$ should not depend on the momentum of the external state. Following Ref. [10] we model the discretization effects using the form $h_B(P^i, P^i) = h_B(P^i = 0, P^i = 0) + r(aP_z^i)^2$. As one can see from Fig. 4 this form describes the data quite well, except for $P_i = 0$. The anomalously large value of $h_B(P^i, P^i)$ at $P_i = 0$ is due to the wrap-around effects as discussed in the previous section. This means that $h_B(P^i, P^i)$ is contaminated by a small contribution proportional to $e^{-aL_t m_\pi}$ mentioned in the previous section. This contribution is also proportional to matrix elements containing two or more pion states with the appropriate qunatum numbers. Constraining such matrix elements is difficult in practice. However, under some physically well motivated assumption it is possible to estimate the corresponding contributions and remove them from $h_B(P^i, P^i)$ [10]. Therefore, we follow the procedure explained in Appendix. A of Ref. [10] to remove this con-

tribution from the matrix element. The corrected result for $h_B(P^i = 0, P^i = 0)$ is shown as the blue point in Fig. 4 and is not very different from the result obtained by the fit. Thus we understand the discretization effects in the forward matrix element $h_B(P^i, P^i)$. We also calculated $Z_V$ for $a = 0.076$ fm using RI-MOM scheme and obtained $Z_V = 0.946(12)$ which agrees with the results on $h_B(P^i = 0, P^i = 0)$ shown in Fig. 4 within errors.

From Fig. 4 we also see that the discretization errors are smaller than 1% for $P_z^i < 1$ GeV and are less than 2% for $P_z^i < 1.6$ GeV. Since the discretization effects as function of $P_z^i$ will be similar for off-forward matrix element it is convenient to obtain the renormalized pion form factor by simply dividing $h_B(P^f, P^i)$ by $h_B(P^i, P^i)$. Then we have $F_\pi(Q^2 = 0) = 1$ by construction and the discretization errors for large $P_z^i$ are removed. We still may have discretization errors proportional $(aQ)^2$. Assuming that these discretization errors are similar to the
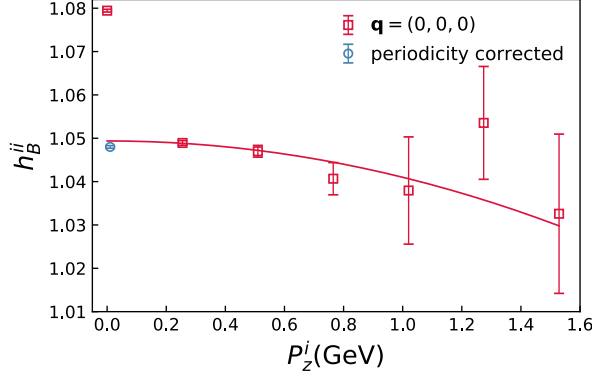
FIG. 4. The forward matrix elements $h_B(P^i, P^i)$. The $P^i_z$ dependence can be described by $h_B(P^i, P^i) = h^{ii}_B(P^i = 0, P^i = 0) + r(aP^i_z)^2$ shown as the line.

$(aP^i_z)^2$ discretization errors we can neglect them. This is because other sources of errors for the form-factors are significantly larger for the considered $Q^2$ range as we will see below.

In Fig. 5, we show the renormalized pion form factors obtained for the $m_\pi = 140$ MeV ensemble and compared to the experimental data CERN [36], as well as the JLAB result [46]. We see good agreement between the lattice results and the experimental data within the estimated error bars at low $Q^2$. It is expected that for low $Q^2$ the pion form factors can be well described by a simple monopole Ansatz motivated by the Vector Meson Dominance (VMD) model [71]

$$F_\pi(Q^2) = \frac{1}{1 + Q^2/M^2}. \tag{8}$$

The monopole mass should be close to the $\rho$ meson mass. Therefore, in Fig. 5 we show the inverse of the pion from factor, $1/F_\pi(Q^2)$ as function of $Q^2$. We see clearly that in the studied range of $Q^2$ the inverse form factor can be well described by a linear function, as expected from monople form, at least up to $Q^2 = 0.4$ GeV The monopole fit of the lattice data (dashed band in Fig. 5) extended to higher $Q^2$ also agrees with the pion form factor obtained by $F_\pi$ collaboration [46], possibly indicating that the monopole form may work in extended range of $Q^2$.

At very low $Q^2$ the the pion form factor can be characterized in terms of the pion charge radius

$$r^2_\pi = -6 \frac{dF_\pi(Q^2)}{dQ^2}\Big|_{Q^2=0}. \tag{9}$$

The pion charge radius is very sensitive to the quark mass. The chiral perturbation predicts that it will diverge logarithmically as pion mass goes to zero [63]. The pion mass dependence is clearly seen in the lattice calculations. In fact, it appears to be challenging to obtain the correct pion charge radius from the lattice results [50–62]. The lattice calculations at the unphysical quark masses lead to smaller pion charge radius than the experimental
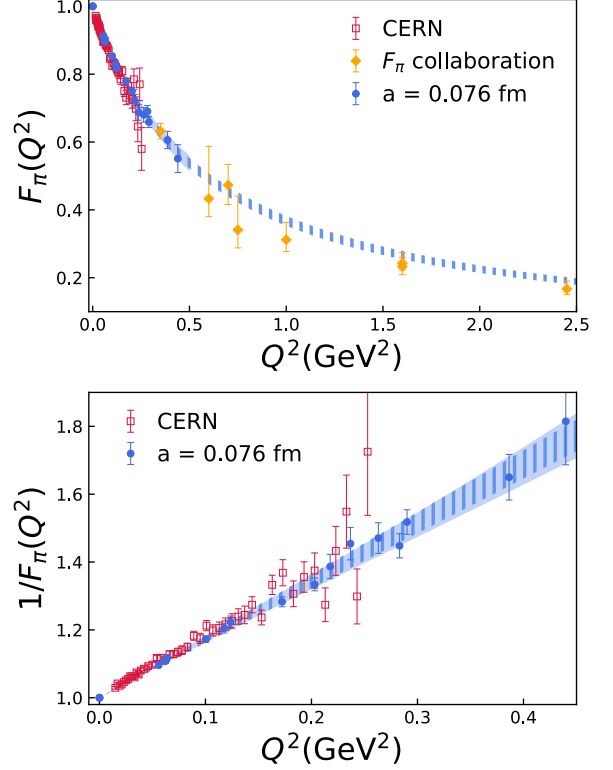




FIG. 5. Pion form factors (upper panel) and the inverse form factors (lower panel) derived from the a = 0.076 fm ($m_\pi = 140$ MeV) ensemble (blue points), compared with the experiment data from CERN (red points) [36] and $F_{pi}$ collaboration (yellow points) [46]. The bands are the fit result of our a = 0.076 fm data, in which the filled band is from $z$-expansion fit and the dashed band is from monopole fit.

results. If the monopole form (8) could describe the pion form factor for all $Q^2$ the pion charge radius would be related to the monopole mass as

$$r_\pi = \sqrt{\frac{6}{M}}. \tag{10}$$

Therefore, it is convenient to represent the lattice results in terms of the effective charge radius defined as [50]

$$r^2_{eff}(Q^2) = \frac{6(1/F_\pi(Q^2) - 1)}{Q^2}. \tag{11}$$

In Fig. 6 we show the effective radius for $a = 0.076$ fm ensemble as well as for the two finer ensembles with $m^{val}_\pi = 300$ MeV. We see from the figure that $r^2_{eff}$ is constant as function of $Q^2$ for all three lattice spacings. For the smallest lattice spacing, $a = 0.04$ fm the results on the effective radius are $Q^2$-independent for $Q^2$ as high as 1.4 GeV. This is consistent with earlier findings [50]. We also clearly see the quark mass dependence of $r^2_{eff}$. The effective radius is smaller for the heavier pion mass as expected. Comparing the results at $a = 0.06$ fm and $a = 0.04$ fm we see no clear lattice spacing dependence
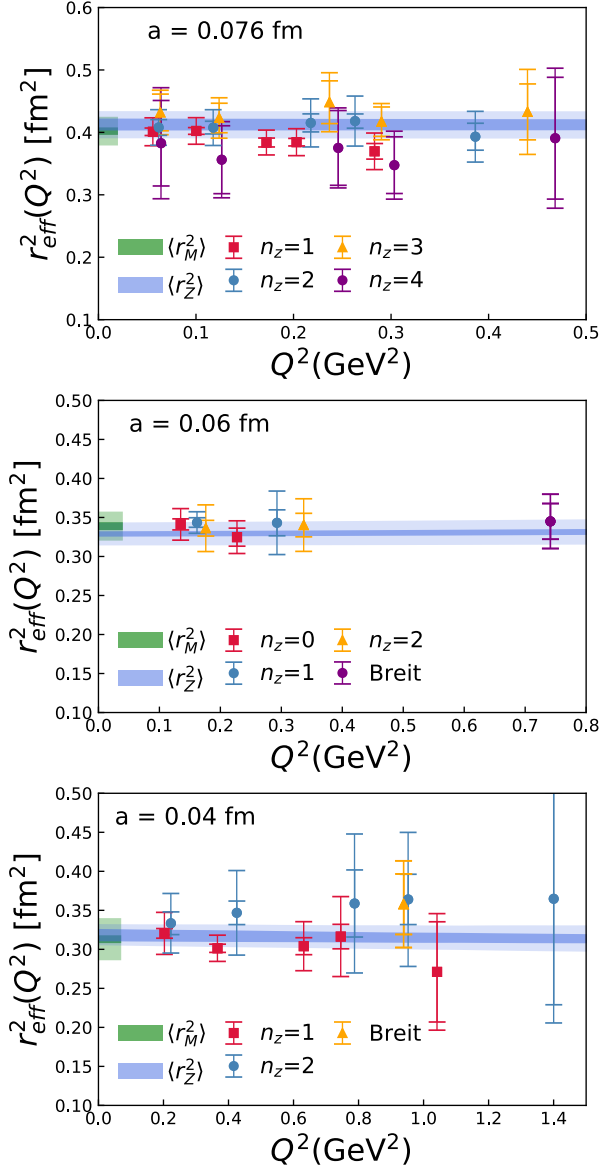
FIG. 6. The effective radius as function of $Q^2$. The smaller error bars are the statistical errors, while the larger error bars also include the systematic errors. We show results for $a = 0.076$ fm (top panel), $a = 0.06$ fm (middle panel) and $a = 0.04$ fm (bottom panel). The blue band is constructed by solving Eq. (9) using $z$-expansion fit results as a function of $Q^2$, while the green band is a constant from monopole fit combining all the form factors.

of $r_{eff}^2$. Therefore, we conclude that for $a = 0.06$ fm the discretization errors for the pion form factor are smaller than the estimated lattice errors in the range of $Q^2$ studied by us. Finally, for the two finer lattices we also show the results from the calculations using Breit frame, which agree with the non Breit frame results.

While the monopole Ansatz seems to describe the pion form factor very well, it is useful to consider an alternative parameterizations of the pion form factor. An

alternative way to fit the form factors is the model independent method called the $z$-expansion. Here the form factor is written as

$$F_\pi(Q^2) = \sum_{k=0}^{k_{max}} a_k z^k$$

$$z(t, t_{\text{cut}}, t_0) = \frac{\sqrt{t_{\text{cut}} - t} - \sqrt{t_{\text{cut}} - t_0}}{\sqrt{t_{\text{cut}} - t} + \sqrt{t_{\text{cut}} - t_0}} \tag{12}$$

where $t = -Q^2$, $a_k$ are the fit parameters with constrain condition $F_\pi(Q^2 = 0) = 1$, and $t_{\text{cut}} = 4m_\pi^2$ is the two-pion production threshold. Furthermore, $t_0$ is chosen to be the optimal value $t_0^{\text{opt}}(Q_{\text{max}}^2) = t_{\text{cut}}(1 - \sqrt{1 + Q_{\text{max}}^2/t_{\text{cut}}})$ to minimize the maximum value of $|z|$, with $Q_{\text{max}}^2$ the maximum $Q^2$ used for the fit. We use AIC model selection rules to determine $k_{max}$, which are 1 for a = 0.06 fm, and 2 for a = 0.04, 0.076 fm data and for the $Q^2$ under consideration. The $z$ expansion results is also shown in Fig. 5 and appear to agree well with the monopole fit, but for larger $Q^2$ it has larger errors, c.f. Fig. 5. We also show the fits with the $z$-expansion in Fig. 6. From this figure we see that this fit works well also for the valence pion mass of 300 MeV and naturally reproduces the $Q^2$ independence of the effective radii. To better understand the quark mass dependence of the pion form factor as well to facilitate the comparison with the experimental results in Fig. 7 we show all the results for the pion form factor in terms of the effective radius $r_{eff}(Q^2)$. We see that the effective radius obtained for the physical pion mass is clearly larger than the one obtained for $m_\pi^{val} = 300$ MeV and is much closer to the CERN data. Furthermore, the fits of $r_{eff}$ for $m_\pi^{val} = 300$ MeV for the two lattice spacing agree within errors. While the individual lattice data and the CERN data appear to agree within errors we also see from the figure that there is a tendency for the CERN data to lie higher than the lattice data. Because the data at different $Q^2$ are correlated this leads so a slight difference in the pion charge radius as discussed below.

The $z$-expansion provides an model independent way to obtain the pion charge radius. In Table III we show the charge pion radius for the three lattice spacings used in our study obtained from the monopole fit and from the $z$-expansion fit. The statistical error are often smaller for the monopole fit, but this fit has larger systematic errors compared to the fit based on $z$-expansion. Within the estimated errors the two fit forms give consistent results. Thus, the model uncertainty in our determination of the pion charge radius is small. As expected the calculations for the heavier quark mass give smaller pion charge radius. As our final estimate of the pion charge radius for physical point we take the result from the $z$-fit:

$$\langle r_\pi^2 \rangle = 0.41(2) \text{ fm}^2, \tag{13}$$

where we added the statistical and systematic errors in quadrature. This result is one sigma lower than the pion charge radius quoted by Particle Data Group (PDG),
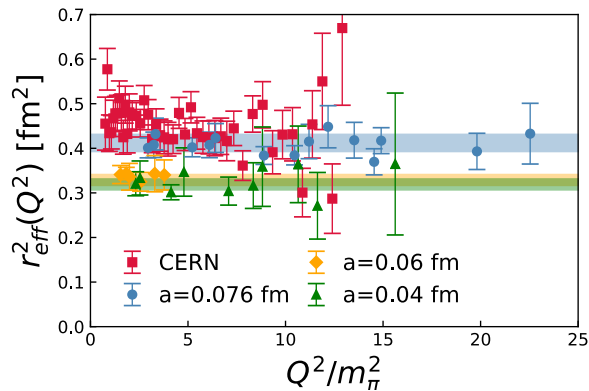
FIG. 7. The comparison of effective radius between CERN and our lattice data as a function of $Q^2/m_\pi^2$. The bands are the z expansion fit results of lattice data (blue, green and orange).

| Data | $n_z$ | $\langle r_M^2 \rangle$ | $\langle r_Z^2 \rangle$ |
|---|---|---|---|
| a=0.076fm | [1,3] | 0.402(6)(23) | 0.412(10)(19) |
| a=0.06fm | [0,3] | 0.339(4)(18) | 0.329(3)(14) |
| a=0.04fm | [1,3] | 0.313(5)(27) | 0.319(9)(11) |

TABLE III. The charge radius computed from monopole fit ($\langle r_M^2 \rangle$) and z-expansion fit ($\langle r_Z^2 \rangle$). The first error is statistical, while the second error is systematic.

$\langle r_\pi^2 \rangle_{\text{PDG}} = 0.434(5)$ fm$^2$ [72], but agrees well with the HPQCD determination that uses HISQ action both in the sea and the valence sector in 2+1+1 flavor QCD, $\langle r_\pi^2 \rangle = 0.403(18)(6)$ fm$^2$ [62]. The most precise lattice determination of the pion charge radius in 2+1 flavor QCD using overlap action in the valence sector and domain wall action in sea has $\langle r_\pi^2 \rangle = 0.436(5)(12)$ fm$^2$ [61]. The 2+1 flavor domain wall calculation gives $\langle r_\pi^2 \rangle = 0.434(20)(13)$ fm$^2$. Finally, the other 2+1 flavor lattice determinations of the pion charge radius have significantly larger errors [58, 59]. Since both our and HPQCD's calculations give lower value of the pion charge radius compared to the PDG value, while calculations with chiral quarks agree very well with with the PDG result we may speculate whether the uncontrolled effects of partial quenching are responsible for this. Calculations at smaller lattice spacing will be needed to clarify this issue.

## VI. CONCLUSIONS

In this paper we studied the pion form factor in 2+1 flavor lattice QCD using three lattices spacings $a = 0.076$, $a = 0.06$ and $a = 0.04$ fm. The calculations on the coarsest lattice have been performed with the physical value of the quark masses, while for the finer two lattices the valence pion mass was 300 MeV. We have found that the pion form factor is very sensitive to the quark mass, as expected. We showed that lattice discretization effects are quite small for lattice spacings smaller than 0.06 fm. For the physical quark masses our lattice results on the pion form factor appear to agree with the experimental determinations. Unlike other lattice studies we also considered highly boosted pions in the initial state using momentum boosted Gaussian sources. In addition we performed calculations also in the Breit frame. We demonstrated that the calculations of the pion form factor performed at different momenta of the pion as well as in the Breit frame give consistent results. This is very important for extending the calculations to pion GPDs.

An important outcome of our analysis is that the monopole Ansatz can describe the pion form factor in large range of $Q^2$, up to $Q^2 = 1.4$ GeV$^2$. In the future it will be important to extend the calculations to even higher momentum transfer given the experimental efforts in Jlab and EIC. To do this we should use boosted sources that also depend on the value of $Q^2$. At present the momentum boost was optimized only according to the pion momentum in the initial state.

From the low $Q^2$ dependence of the pion form factor we determined the pion charge radius, which is one sigma lower that the experimental result. We speculated, whether this is due to the effect of partial quenching. To fully resolve this issue calculations at smaller lattice spacing with the physical value of the pion masses are needed.

[1] Z.-F. Cui, M. Ding, F. Gao, K. Raya, D. Binosi, L. Chang, C. D. Roberts, J. Rodríguez-Quintero, and S. M. Schmidt, Eur. Phys. J. A **57**, 5 (2021), arXiv:2006.14075 [hep-ph].

[2] C. D. Roberts and S. M. Schmidt, Eur. Phys. J. ST **229**, 3319 (2020), arXiv:2006.08782 [hep-ph].

[3] P. C. Barry, N. Sato, W. Melnitchouk, and C.-R. Ji, Phys. Rev. Lett. **121**, 152001 (2018), arXiv:1804.01965 [hep-ph].

[4] I. Novikov *et al.*, Phys. Rev. D **102**, 014040 (2020), arXiv:2002.02902 [hep-ph].

[5] J.-H. Zhang, J.-W. Chen, L. Jin, H.-W. Lin, A. Schäfer, and Y. Zhao, Phys. Rev. D **100**, 034505 (2019), arXiv:1804.01483 [hep-lat].

[6] R. S. Sufian, J. Karpie, C. Egerer, K. Orginos, J.-W. Qiu, and D. G. Richards, Phys. Rev. D **99**, 074507 (2019), arXiv:1901.03921 [hep-lat].

[7] B. Joó, J. Karpie, K. Orginos, A. V. Radyushkin, D. G. Richards, R. S. Sufian, and S. Zafeiropoulos, Phys. Rev. D **100**, 114512 (2019), arXiv:1909.08517 [hep-lat].

[8] R. S. Sufian, C. Egerer, J. Karpie, R. G. Edwards, B. Joó, Y.-Q. Ma, K. Orginos, J.-W. Qiu, and D. G. Richards, Phys. Rev. D **102**, 054508 (2020), arXiv:2001.04960 [hep-lat].

[9] T. Izubuchi, L. Jin, C. Kallidonis, N. Karthik, S. Mukherjee, P. Petreczky, C. Shugert, and S. Syritsyn, Phys. Rev. D **100**, 034516 (2019), arXiv:1905.06349 [hep-lat].

[10] X. Gao, L. Jin, C. Kallidonis, N. Karthik, S. Mukherjee, P. Petreczky, C. Shugert, S. Syritsyn, and Y. Zhao, Phys. Rev. D **102**, 094513 (2020), arXiv:2007.06590 [hep-lat].

[11] X. Ji, Phys. Rev. Lett. **110**, 262002 (2013), arXiv:1305.1539 [hep-ph].

[12] X. Ji, Sci. China Phys. Mech. Astron. **57**, 1407 (2014), arXiv:1404.6680 [hep-ph].

[13] A. V. Radyushkin, Phys. Rev. D **96**, 034025 (2017), arXiv:1705.01488 [hep-ph].

[14] K. Orginos, A. Radyushkin, J. Karpie, and S. Zafeiropoulos, Phys. Rev. D **96**, 094503 (2017), arXiv:1706.05373 [hep-ph].

[15] V. Braun and D. Müller, Eur. Phys. J. C **55**, 349 (2008), arXiv:0709.1348 [hep-ph].

[16] Y.-Q. Ma and J.-W. Qiu, Phys. Rev. D **98**, 074021 (2018), arXiv:1404.6860 [hep-ph].

[17] Y.-Q. Ma and J.-W. Qiu, Phys. Rev. Lett. **120**, 022003 (2018), arXiv:1709.03018 [hep-ph].

[18] K. Cichy and M. Constantinou, Adv. High Energy Phys. **2019**, 3036904 (2019), arXiv:1811.07248 [hep-lat].

[19] Y. Zhao, Int. J. Mod. Phys. A **33**, 1830033 (2019), arXiv:1812.07192 [hep-ph].

[20] A. V. Radyushkin, Int. J. Mod. Phys. A **35**, 2030002 (2020), arXiv:1912.04244 [hep-ph].

[21] X. Ji, Y.-S. Liu, Y. Liu, J.-H. Zhang, and Y. Zhao, (2020), arXiv:2004.03543 [hep-ph].

[22] C. Best, M. Gockeler, R. Horsley, E.-M. Ilgenfritz, H. Perlt, P. E. L. Rakow, A. Schafer, G. Schierholz, A. Schiller, and S. Schramm, Phys. Rev. D **56**, 2743 (1997), arXiv:hep-lat/9703014.

[23] M. Guagnelli, K. Jansen, F. Palombi, R. Petronzio, A. Shindler, and I. Wetzorke (Zeuthen-Rome (ZeRo)), Eur. Phys. J. C **40**, 69 (2005), arXiv:hep-lat/0405027.

[24] S. Capitani, K. Jansen, M. Papinutto, A. Shindler, C. Urbach, and I. Wetzorke, Phys. Lett. B **639**, 520 (2006), arXiv:hep-lat/0511013.

[25] A. Abdel-Rehim *et al.*, Phys. Rev. D **92**, 114513 (2015), [Erratum: Phys.Rev.D 93, 039904 (2016)], arXiv:1507.04936 [hep-lat].

[26] M. Oehm, C. Alexandrou, M. Constantinou, K. Jansen, G. Koutsou, B. Kostrzewa, F. Steffens, C. Urbach, and S. Zafeiropoulos, Phys. Rev. D **99**, 014508 (2019), arXiv:1810.09743 [hep-lat].

[27] C. Alexandrou, S. Bacchio, I. Cloet, M. Constantinou, K. Hadjiyiannakou, G. Koutsou, and C. Lauer, Phys. Rev. D **103**, 014508 (2021), arXiv:2010.03495 [hep-lat].

[28] J. Dudek *et al.*, Eur. Phys. J. A **48**, 187 (2012), arXiv:1208.1244 [hep-ex].

[29] Y.-S. Liu, W. Wang, J. Xu, Q.-A. Zhang, J.-H. Zhang, S. Zhao, and Y. Zhao, Phys. Rev. D **100**, 034006 (2019), arXiv:1902.00307 [hep-ph].

[30] J.-W. Chen, H.-W. Lin, and J.-H. Zhang, Nucl. Phys. B **952**, 114940 (2020), arXiv:1904.12376 [hep-lat].

[31] H.-W. Lin, (2020), arXiv:2008.12474 [hep-ph].

[32] C. Alexandrou, K. Cichy, M. Constantinou, K. Hadjiyiannakou, K. Jansen, A. Scapellato, and F. Steffens, Phys. Rev. Lett. **125**, 262001 (2020), arXiv:2008.10573 [hep-lat].

[33] E. B. Dally *et al.*, Phys. Rev. D **24**, 1718 (1981).

[34] E. B. Dally *et al.*, Phys. Rev. Lett. **48**, 375 (1982).

[35] S. R. Amendolia *et al.*, Phys. Lett. B **146**, 116 (1984).

[36] S. Amendolia *et al.* (NA7), Nucl. Phys. B **277**, 168 (1986).

[37] C. J. Bebek, C. N. Brown, M. Herzlinger, S. D. Holmes, C. A. Lichtenstein, F. M. Pipkin, S. Raither, and L. K. Sisterson, Phys. Rev. D **13**, 25 (1976).

[38] C. J. Bebek *et al.*, Phys. Rev. Lett. **37**, 1326 (1976).

[39] C. J. Bebek *et al.*, Phys. Rev. D **17**, 1693 (1978).

[40] H. Ackermann, T. Azemoon, W. Gabriel, H. D. Mertiens, H. D. Reich, G. Specht, F. Janata, and D. Schmidt, Nucl. Phys. B **137**, 294 (1978).

[41] P. Brauel, T. Canzler, D. Cords, R. Felst, G. Grindhammer, M. Helm, W. D. Kollmann, H. Krehbiel, and M. Schadlich, Z. Phys. C **3**, 101 (1979).

[42] J. Volmer *et al.* (Jefferson Lab F(pi)), Phys. Rev. Lett. **86**, 1713 (2001), arXiv:nucl-ex/0010009.

[43] V. Tadevosyan *et al.* (Jefferson Lab F(pi)), Phys. Rev. C **75**, 055205 (2007), arXiv:nucl-ex/0607007.

[44] T. Horn *et al.* (Jefferson Lab F(pi)-2), Phys. Rev. Lett. **97**, 192001 (2006), arXiv:nucl-ex/0607005.

[45] H. P. Blok *et al.* (Jefferson Lab), Phys. Rev. C **78**, 045202 (2008), arXiv:0809.3161 [nucl-ex].

[46] G. Huber *et al.* (Jefferson Lab), Phys. Rev. C **78**, 045203 (2008), arXiv:0809.3052 [nucl-ex].

[47] G. P. Lepage and S. J. Brodsky, Phys. Lett. B **87**, 359 (1979).

[48] G. Martinelli and C. T. Sachrajda, Nucl. Phys. B **306**, 865 (1988).

[49] T. Draper, R. M. Woloshyn, W. Wilcox, and K.-F. Liu, Nucl. Phys. B **318**, 319 (1989).

[50] D. Brömmel *et al.* (QCDSF/UKQCD), Eur. Phys. J. C **51**, 335 (2007), arXiv:hep-lat/0608021.

[51] R. Frezzotti, V. Lubicz, and S. Simula (ETM), Phys. Rev. D **79**, 074506 (2009), arXiv:0812.4042 [hep-lat].

[52] S. Aoki *et al.* (JLQCD, TWQCD), Phys. Rev. D **80**, 034508 (2009), arXiv:0905.2465 [hep-lat].

[53] B. B. Brandt, A. Jüttner, and H. Wittig, JHEP **11**, 034 (2013), arXiv:1306.2916 [hep-lat].

[54] C. Alexandrou *et al.* (ETM), Phys. Rev. D **97**, 014508 (2018), arXiv:1710.10401 [hep-lat].

[55] F. D. R. Bonnet, R. G. Edwards, G. T. Fleming, R. Lewis, and D. G. Richards (Lattice Hadron Physics), Phys. Rev. D **72**, 054506 (2005), arXiv:hep-lat/0411028.

[56] P. A. Boyle, J. M. Flynn, A. Juttner, C. Kelly, H. P. de Lima, C. M. Maynard, C. T. Sachrajda, and J. M. Zanotti, JHEP **07**, 112 (2008), arXiv:0804.3971 [hep-lat].

[57] O. H. Nguyen, K.-I. Ishikawa, A. Ukawa, and N. Ukita, JHEP **04**, 122 (2011), arXiv:1102.3652 [hep-lat].

[58] H. Fukaya, S. Aoki, S. Hashimoto, T. Kaneko, H. Matsufuru, and J. Noaki, Phys. Rev. D **90**, 034506 (2014), arXiv:1405.4077 [hep-lat].

[59] S. Aoki, G. Cossu, X. Feng, S. Hashimoto, T. Kaneko, J. Noaki, and T. Onogi (JLQCD), Phys. Rev. D **93**, 034504 (2016), arXiv:1510.06470 [hep-lat].

[60] X. Feng, Y. Fu, and L.-C. Jin, Phys. Rev. D **101**, 051502 (2020), arXiv:1911.04064 [hep-lat].

[61] G. Wang, J. Liang, T. Draper, K.-F. Liu, and Y.-B. Yang (chiQCD), (2020), arXiv:2006.05431 [hep-ph].

[62] J. Koponen, F. Bursa, C. Davies, R. Dowdall, and G. Lepage, Phys. Rev. D **93**, 054503 (2016), arXiv:1511.07382 [hep-lat].

[63] J. Bijnens, G. Colangelo, and P. Talavera, JHEP **05**, 014 (1998), arXiv:hep-ph/9805389.

[64] A. Hasenfratz and F. Knechtli, Phys. Rev. D **64**, 034504 (2001), arXiv:hep-lat/0103029.

[65] A. Bazavov *et al.* (HotQCD), Phys. Rev. D **90**, 094503 (2014), arXiv:1407.6387 [hep-lat].

[66] A. Bazavov *et al.*, Phys. Rev. D **100**, 094510 (2019), arXiv:1908.09552 [hep-lat].

[67] A. Bazavov *et al.* (MILC), PoS **LATTICE2010**, 074 (2010), arXiv:1012.0868 [hep-lat].

[68] E. Shintani, R. Arthur, T. Blum, T. Izubuchi, C. Jung, and C. Lehner, Phys. Rev. D **91**, 114511 (2015), arXiv:1402.0244 [hep-lat].

[69] X. Gao, N. Karthik, S. Mukherjee, P. Petreczky, S. Syritsyn, and Y. Zhao, (2021), arXiv:2101.11632 [hep-lat].

[70] S. Capitani *et al.*, Nucl. Phys. B Proc. Suppl. **73**, 294 (1999), arXiv:hep-lat/9809172.

[71] H. B. O'Connell, B. C. Pearce, A. W. Thomas, and A. G. Williams, Phys. Lett. B **354**, 14 (1995), arXiv:hep-ph/9503332.

[72] P. A. Zyla *et al.* (Particle Data Group), PTEP **2020**, 083C01 (2020).